Soft Matter

PAPER

View Article Online
View Journal | View Issue



Cite this: *Soft Matter*, 2025, **21**, 8379

# Geometrical factors govern ballistic energy dissipation of polymeric nanoscale thin films

Laureano Ortellado, *[ab] Nicolás A. García,[b] Gabriel Catalini,[b] Jean-Louis Barrat[a] and Leopoldo R. Gómez[b]

Received 18th June 2025,
Accepted 14th October 2025

DOI: 10.1039/d5sm00618j

rsc.li/soft-matter-journal

The design of materials with enhanced resistance to impact and shock deformation is critical for numerous technological applications. This work investigates energy dissipation mechanisms in ballistic impacts on nanoscale polymer thin films through molecular dynamics simulations and theoretical modeling. Using a pseudo-continuous model for polymer chain generation followed by Kremer–Grest potential relaxation, we systematically study the effects of impact velocity, projectile radius, and film thickness for various polymer chain lengths. Our findings reveal that traditional kinetic impact models are insufficient to describe the observed energy dissipation. We propose an improved model incorporating an energy dissipation term that scales with the cylindrical hole area created during impact, characterized by a single fitting parameter $\beta$, that encapsulates shear-dependent deformation and failure mechanisms. This model accurately predicts energy dissipation across both low and high-velocity regimes and shows that energy dissipation scales linearly with film thickness at the nanoscale.



## 1 Introduction

The development of novel materials resistant to impact and shock waves is of great importance across various industries. For instance, cavitation causes wear in pipes and turbines,[1] impacts from small space debris can damage satellites or windows of space stations,[2] and aircraft turbines may be compromised by atmospheric particles.[3,4] Coating surfaces with thin polymer films is a promising approach offering several advantages, including lightweight design, transparency, low cost, and shear-rate-dependent mechanical properties.[5,6] Notably, laser-induced projectile impact tests (LIPIT) have demonstrated that polymer thin films exhibit superior impact absorption compared to materials such as metals or multilayer graphene.[7] This motivates further exploration into the energy absorption mechanisms within polymer thin films.

In general, the impact response of polymer thin films is a complex phenomenon influenced by multiple factors. For example, the entanglement density of polymer chains has been shown to positively correlate with ballistic energy absorption.[8,9] Additionally, Cai and Thevamaran demonstrated that the degree of crystallinity strongly affects the specific penetration energy,[10] while molecular dynamics simulations by Gürel *et al.* suggest that polydispersity can also affect ballistic energy absorption.[11]

In a simplified kinetic model,[12] the impact is treated as an inelastic collision between the projectile and a plug of the thin film, which is ejected at the same residual velocity ($v_r$) as the projectile after the impact. The energy balance is then expressed as:

$$\frac{1}{2}m_p v_i^2 = \frac{1}{2}(m_p + m_f)v_r^2 + E_d, \quad (1)$$

where $m_p$ and $m_f$ are the masses of the projectile and film plug, respectively, $v_i$ is the impact velocity, and $E_d$ comprises all other energy dissipation mechanisms, including heat and sound generation, film deformation, and crack formation.[13] Equivalently, by defining $\alpha = \frac{m_p}{m_p + m_f}$ and $\gamma = \frac{2E_d}{m_p + m_f}$, one may model the dissipated kinetic energy *via*: $v_r^2 = \alpha v_i^2 - \gamma$.

The mass of the film plug is typically approximated as the mass contained within the projectile's strike area, $m_f = 2\pi R_p^2 H\rho$, where $R_p$ is the projectile radius, and $H$ and $\rho$ are the film thickness and density, respectively. Although the impact creates tensile and transverse waves that extend beyond the immediate strike area,[14,15] we will demonstrate that this simple model for $m_f$ yields quantitatively reliable results. Chen *et al.* studied the dissipation mechanisms in polymeric thin films using microscale projectiles.[13] By comparing their results with experimental data, they concluded that fracture work and plastic yielding are the primary energy dissipation modes, especially at low film thicknesses. They introduced an

[a] Univ. Grenoble Alpes, CNRS, LIPhy, 38000 Grenoble, France. E-mail: laureano.ortellado@univ-grenoble-alpes.fr
[b] Instituto de Física del Sur (IFISUR), Departamento de Física, Universidad Nacional del Sur (UNS), CONICET, Av. L. N. Alem 1253, B8000CPB-Bahía Blanca, Argentina

energy contribution scaling as $\sim H^2$ to account for fracture work.

Meng and Keten conducted ballistic impact molecular dynamics simulations on four different materials, including polymer thin films.[16] They investigated the effects of material density, mechanical properties, and geometric factors on dissipated energy. Their findings indicate that mechanical properties predominantly influence energy dissipation at low $v_i$, while material density tends to dominate at high $v_i$.

In this work, we investigate ballistic energy dissipation mechanisms in nanoscale polymer thin films through numerical simulations. In order to interpret the results beyond the simplified kinetic model, we incorporate an energy dissipation term scaling with the area of the cylindrical hole created during impact. This model features a single fitting parameter encapsulating shear-dependent deformation and failure mechanisms. Our model is validated against extensive impact simulations spanning a broad range of impact velocities, projectile radii, and film thicknesses. Our results establish a unified framework applicable to both low- and high-velocity impacts, demonstrating that the appropriate energy dissipation scaling at the nanoscale is $\sim H$.

# 2 Simulation model

## 2.1 Pseudo-continuous model

The simulation of highly entangled polymers poses the challenge of relaxing long polymer chains, which would result in inaccessible simulation times when using standard models like Kremer–Grest. For this reason, a pseudo-continuous model of polymer solutions has been chosen, in which the chains interact *via* a soft potential field.[17] This novel model of entangled polymer solutions has proven effective in simulating polymer brushes under shear flows,[18] star polymer solutions,[19] and, particularly relevant to our work, thin polymer films.[20]

The motion of chains $C$, each described by a continuous curve $\mathbf{R}_c(t,s)$ with variables $t$ for time and $s \in (0,1)$ as the monomer index, is solved numerically. $s$ uses a finite number of discrete points $j = 1, 2, \ldots, J$ to oversample the chains. Choosing $J = N$, the chain reduces to the standard spring model, which, for this soft potential, has gaps that may allow chains to cross each other. Crossings are avoided by sufficiently oversampling the chains to effectively suppress gaps along the polymer. In this work, we use $N = J/4$ as it is sufficient to accurately describe the chains in all our simulations, avoiding phantom crossings between the chains. In contrast, higher-resolution sampling would unnecessarily slow down the simulations.

Each chain has $N$ degrees of freedom corresponding to the usual Rouse modes and follows the first-order stochastic equation of motion:

$$\zeta \frac{\partial \mathbf{R}_c(t,s)}{\partial t} = F_s - N\nabla V_c + \sqrt{2k_B T\zeta}\mathbf{W}_c(t,c) \qquad (2)$$

where $\zeta = N\zeta_0$ is the friction coefficient of the chain's center of mass. The thermal noise force is modeled by a Wiener process $\langle \mathbf{W}_c(t,c)\mathbf{W}_{c'}(t',c')\rangle = \delta_{cc'}\delta(t-t')\delta(s-s')$.

In eqn (2), $F_s$ models the bond interaction *via* $F_s = \left(\frac{3k_bT}{Nb^2}\frac{\partial^2 \mathbf{R}_c(t,s)}{\partial s^2}\right)$, where $Nb^2$ is the mean square end-to-end distance of a free chain and can be combined with other parameters to define the microscopic time unit, $\tau = \zeta_0 b^2/k_bT$. $V_c$ describes the chain interaction:

$$V_c = \sum_{c'=1}^{C}\int_0^1 \Phi[R_c(t,s) - R_{c'}(t',s')]\mathrm{d}s' \qquad (3)$$

The soft potential $\Phi(r)$ combines a Gaussian function simulating an excluded volume potential with an attractive potential:

$$\Phi(r) = \frac{N}{J}k_bT\left[(w+1)\mathrm{e}^{-r^2/2\sigma^2} - w\mathrm{e}^{-r^2/4\sigma^2}\right] \qquad (4)$$

where $w$ is a parameter controlling the relative weight of the attractive part of the potential and takes the value $w = 0.5$ in this work, ensuring thermodynamic stability. More details on the pseudo-continuous model can be found in ref. 20.

The initial configuration begins by randomly placing $C$ monomers in a periodic boundary conditions box of appropriate size to achieve the desired thin film dimensions. Initially, each chain has a single monomer. As the simulation progresses, monomers are systematically added along the chain, rescaling the box to preserve the polymer solution density. This process is repeated until the desired chain length is reached. The attractive potential, dominated by the parameter $w$, leads to the spontaneous formation of a thin film.

## 2.2 Kremer–Grest model

Impact simulations require a polymer model with potentials stable under high shear rates. The Kremer–Grest model is a simple, computationally efficient, and successful model for simulating polymer responses to shock waves.[21–23] Impact simulations were performed using the open-source molecular dynamics program HOOMD-Blue.[24]

Thus, once the initial configuration of the thin polymer films has been generated using the pseudo-continuous potential, the system is relaxed using a generalized version of the Kremer–Grest model. This consists of a truncated and shifted Lennard-Jones (LJTS) potential used to model the interaction between two monomers at a distance $r$:[25]

$$U_{\mathrm{LJTS}}(r) = \begin{cases} 4\varepsilon_{ij}\left[\left(\frac{\sigma}{r}\right)^{12} - \left(\frac{\sigma}{r}\right)^{6}\right] + \delta, & r \le r_c \\ 0, & r > r_c \end{cases} \qquad (5)$$

where $\varepsilon_{ij}$ is the interaction strength between two particles $i$ and $j$, $\sigma$ represents the diameter of a monomer, $r_c = 2.5\sigma$ is the potential cutoff distance, and $\delta$ is the value of the Lennard-Jones potential at $r = r_c$. In this work, all results are reported in reduced units where $\sigma = 1$, the energy parameter $\varepsilon = 1$, and the particle mass $m = 1$. The strength of the interaction is determined by the parameter $\varepsilon_{ij}$, defined as $\varepsilon_{ij} = 1\varepsilon$.

Additionally, adjacent monomers along the chain are connected through a finite extensible non-linear elastic potential

 

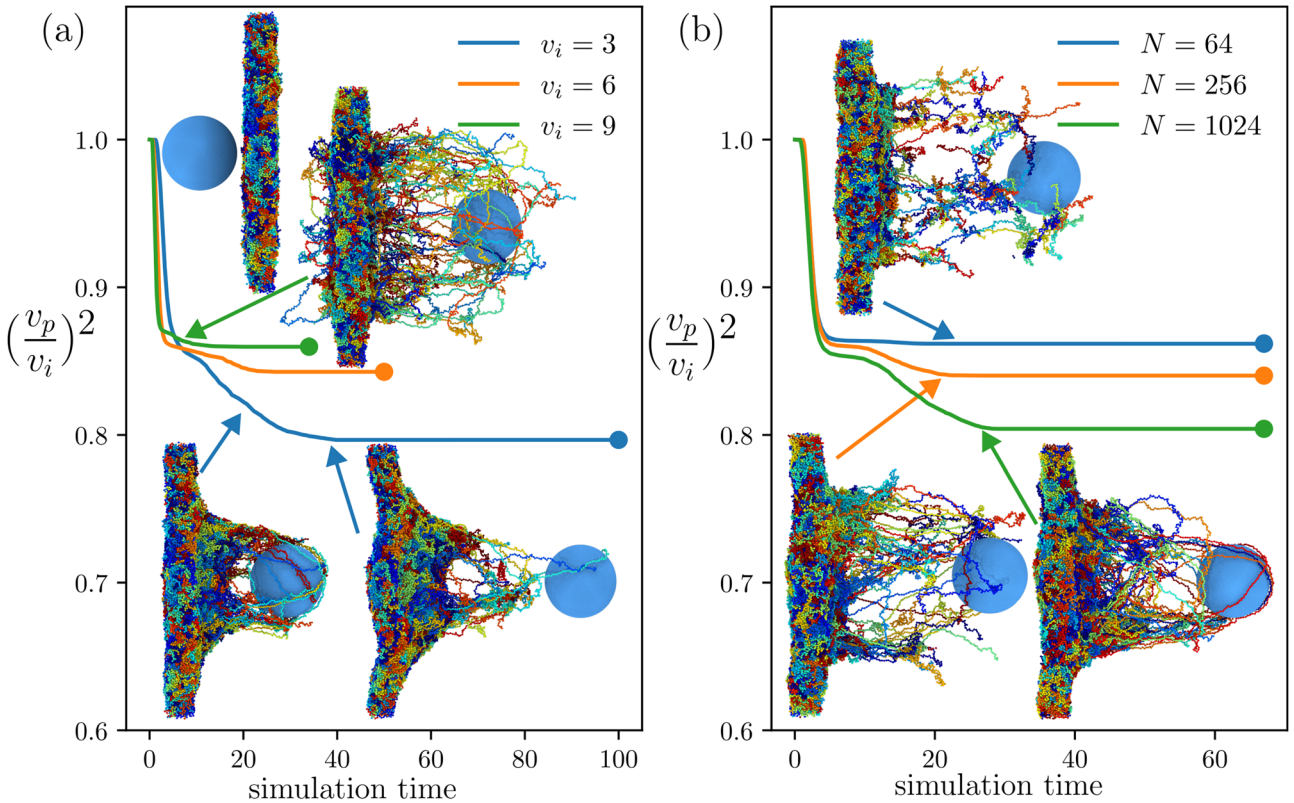


Fig. 1 Normalized projectile kinetic energy profiles and simulation snapshots of projectile impacts. (a) Kinetic energy profiles for three different impact velocities ($v_i$) on the same thin film ($N$ = 256). (b) Kinetic energy profiles for three films with different polymer chain lengths at a fixed impact velocity of $v_i$ = 4.5. All simulations are performed with $\alpha$ = 0.9, $R_p$ = 15 and $H$ = 11.

(FENE) defined as:

$$U_{\mathrm{FENE}}(r) = \begin{cases} -\frac{1}{2}kR_0^2 \ln\left[1 - \left(\frac{r}{R_0}\right)^2\right], & r \le R_0 \\ \infty, & r > R_0 \end{cases} \quad (6)$$

where $k = 30(\varepsilon/\sigma^2)$ and $R_0 = 1.5\sigma$.[25–27] This specific choice prevents chains from crossing each other.

The transition between the two models leads to a decrease in the film thickness. Finally, the thin film reaches a mass density of $\rho \approx 0.87m\sigma^{-3}$. During the transition between the two models, the topology of the entanglement network is preserved.

The simulation snapshot in Fig. 1(a) shows the initial configuration of the impact on a thin film. The projectile is modeled as a rigid spherical shell, constructed as a spherical polyhedron whose vertices are occupied by particles interacting *via* a purely repulsive Lennard-Jones potential (eqn (5)), truncated at a cutoff radius $r_c = 2^{1/6}\sigma$. This choice prevents any adhesive interactions with the polymeric thin films, thereby precluding additional chain pull-out that may occur in real systems, especially at low-velocity impacts.[28] The number of particles comprising the spherical shell of the projectile varies according to its radius, ensuring a particle surface density exceeding $3.6\sigma^{-2}$, such that the results are independent of the discretization. The projectile mass can be varied independently of its size and, in most simulations, rescaled to preserve a constant value of the parameter $\alpha$. For simplicity, the possible rotation of the projectile during the impact is neglected. The addition of projectile rotation, although potentially relevant in some systems, does not affect our results, as the films are sufficiently homogeneous to prevent an effective torque from developing during impact.

The size of the simulation box is described in Table 1. In the direction of impact, the box has a length $L_z = 400\sigma$. Since impacts are short-duration events, they are modeled as adiabatic processes. Consequently, impact simulations are performed in a adiabatic (NVE) ensemble. To ensure the stability of the simulations during impact, a small timestep $\Delta t = 1 \times 10^{-4}\tau$ is selected.

Table 1 Dimensions of polymer thin films used in impact simulations, indicating film thickness ($H$) and corresponding lateral dimensions ($L_x$, $L_y$). All lengths are expressed in units of $\sigma$

| Thickness, $H$ | Lateral size, $L_x = L_y$ |
|---|---|
| 11.0 | 82.0 |
| 14.0 | 103.0 |
| 17.5 | 130.0 |
| 21.2 | 118.0 |
| 25.5 | 107.5 |
| 29.5 | 100.0 |

# 3 Results

## 3.1 Simulations

Since the dynamic response of a polymer chain depends on its molecular weight, nanoparticle impacts were simulated for thin films composed of polymer chains with lengths of $N = 2^n$, where $n$ ranges from 6 to 10. This exponential spacing of chain lengths ensures rapid convergence of the pseudo-continuous model. Impacts are generated by releasing the projectile at an initial velocity $v_i$, varying from 3 to 9, from an initial distance of $2\sigma$ to avoid prior interactions. The momentum transfer due to the projectile-film interaction initially reduces the projectile's velocity $v_p$. Panel (a) of Fig. 1 shows impacts at three initial velocities on a film composed of chains with $N = 256$. At higher velocities, rapid kinetic energy transfer occurs between projectile and film, while at lower velocities, energy transfer is more gradual and substantial relative to the initial kinetic energy.

At high impact velocities, the collision generates a shock wave traveling at velocity $v_s$, greater than the projectile velocity ($v_s > v_p$). This shock wave ejects film material ahead of the projectile, as evidenced by simulation snapshots. Consequently, the projectile-film interaction is brief, ending once sufficient energy is transferred to form the shock wave.[29]

In contrast, low-velocity impacts cause polymers to wrap around the projectile, requiring disentanglement for projectile progression, as seen in simulation snapshots. This leads to prolonged interactions and more irregular normalized kinetic energy profiles. Similar results were reported by Bowman *et al.* in atomistic simulations of nanoparticle impacts on thin polyethylene and polystyrene films.

Panel (b) of Fig. 1 illustrates impacts on films with varying polymer lengths at a fixed velocity $v_i = 4.5$. Despite different chain lengths, normalized kinetic energy profiles appear initially similar. Short-chain polymers exhibit weak entanglement, requiring minimal energy for displacement, leading to sharp yet shallow kinetic energy profiles. Conversely, longer polymer chains have greater mass and stronger entanglement, requiring more energy for displacement. These chains wrap around the projectile, resulting in irregular and more pronounced kinetic energy variations, indicating higher energy absorption. The final projectile velocity after interaction defines the residual velocity $v_r$, indicated by circles in Fig. 1. The ratio $(v_r/v_i)^2$ quantifies the fraction of projectile residual kinetic energy so that the fraction of dissipated energy is $1 - (v_r/v_i)^2$.

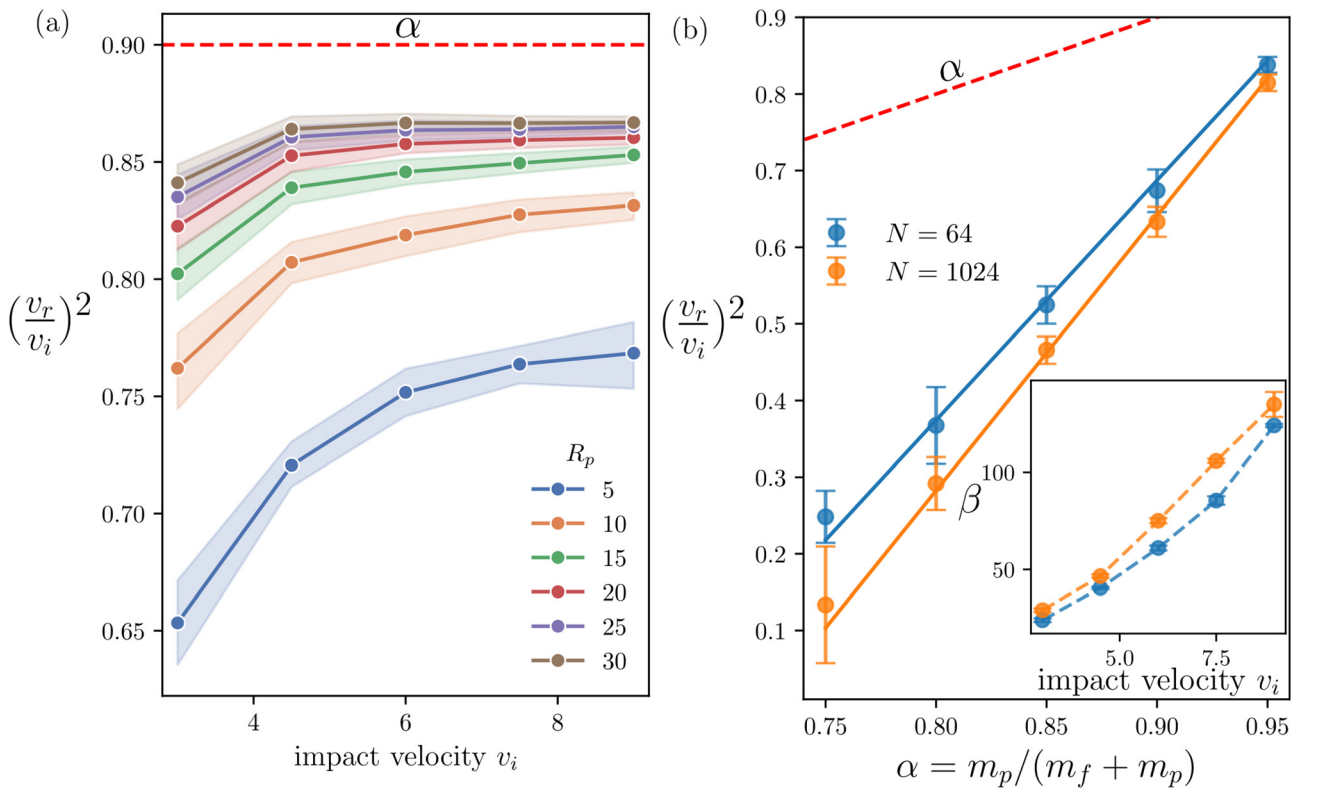


Fig. 2 (a) Kinetic energy dissipation as a function of impact velocity and projectile radius $R_p$. The film thickness is $H = 11$ and the results are averaged over all chain length. (b) Dissipated energy as a function of $\alpha$ for different chain lengths $N$ at $H = 11$ and $R_p = 5$. Symbols represent simulation data, and solid lines represent fits using the function $\alpha - \beta(v_i, N)\frac{4(1-\alpha)}{R_p v_i^2}$, where $\beta$ is the fitting parameter. For panel (b), $v_i = 3$. The inset of panel (b) shows the variation of $\beta$ with impact velocity, and the dashed red line represents the kinetic energy dissipation considering only momentum transfer with the film plug mass $m_f$. Error bars represent one standard deviation.

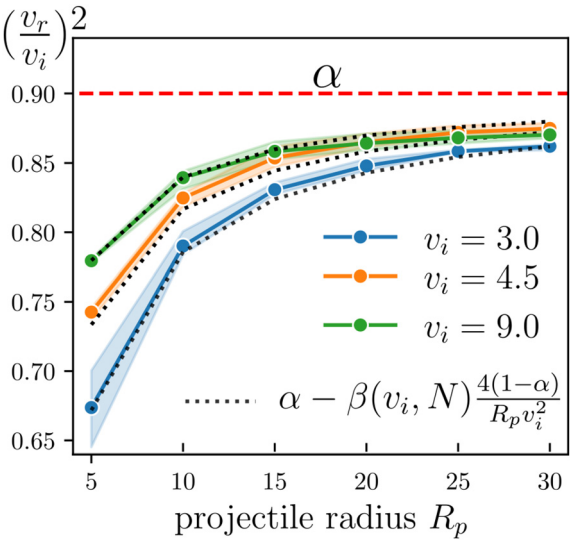


Fig. 3 Residual projectile kinetic energy as a function of projectile radius $R_p$ for different impact velocities $v_i$, using $N = 64$ and $H = 11$. Shaded regions represent one standard deviation.

### 3.2 Simplified modeling

Fig. 2(a) illustrates the kinetic energy variation for different impact velocities and projectile radii, with $\alpha = \frac{m_p}{m_p + m_f}$ fixed at 0.9. Considering only the energy dissipation due to momentum transfer $\left(\frac{v_r}{v_i}\right)^2 \equiv \alpha$ (red dashed line) does not fully explain the observed kinetic energy loss. Moreover, there is a clear dependence on projectile radius not captured by conventional kinetic descriptions. Fig. 2(b) displays the fraction of residual kinetic energy as a function of $\alpha$, varied by changing the projectile mass. It is clearly seen that the simulation results deviate significantly from the traditional kinetic model, especially at low $\alpha$, where dissipation increases notably.

Meng and Keten demonstrated that, at low velocities, dissipated energy scales more closely with the projectile circumference ($\sim R_p$) rather than its projected area ($\sim R_p^2$), due to a tearing mechanism.[16] Inspired by this, we propose that energy dissipation scales with the cylindrical hole area created upon impact, leading to $E_d = \beta \times 2\pi R_p H \rho$, where $\beta(v_i,N)$ is a prefactor discussed below. Consequently, the dissipated kinetic energy is expressed, using $m_f = \pi\rho H R_p^2$, as:

$$\left(\frac{v_r}{v_i}\right)^2 = \alpha - \beta(v_i, N)\frac{4(1-\alpha)}{R_p v_i^2}. \quad (7)$$

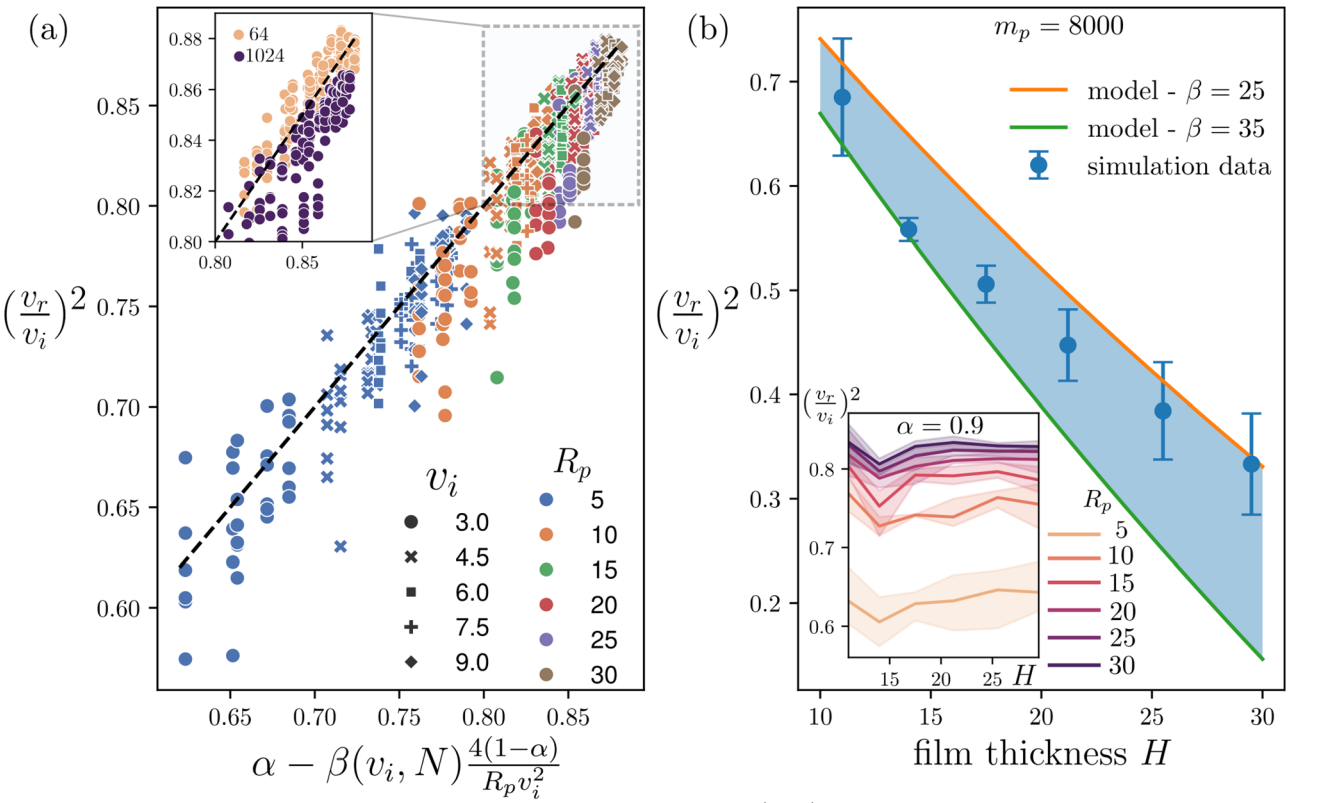


Fig. 4 Kinetic energy dissipation as a function of (a) the proposed formula $\alpha - \beta(v_i, N)\frac{4(1-\alpha)}{R_p v_i^2}$ for film thicknesses $H = 11$ and $H = 14$. The dashed line represents the identity function. For each parameter set, three independent simulations were conducted, totaling 900 simulations. Here $\alpha = 0.9$. The inset highlights results for two representative $N$ values. Panel (b) presents kinetic energy dissipation *versus* film thickness $H$ for constant projectile mass $m_p = 8000$, chain length $N = 512$, $R_p = 5$, and $v_i = 3$. Simulation data lie between theoretical predictions using two estimated $\beta$ values from Fig. 2(b). The inset shows kinetic energy dissipation *versus* film thickness for constant $\alpha$ and varying $R_p$. Error bars indicate one standard deviation.

To determine $\beta$, data for each $N$ and $v_i$ were fitted using eqn (7) for different values of $\alpha$, as shown in Fig. 2(b). Although there is some scatter in the data, the agreement between the model and numerical simulations is satisfactory. The mechanical response of polymeric materials strongly depends on strain rate and polymerization degree, thus the dissipation expressed by the parameter $\beta(v_i,N)$ naturally increases with both $N$ and impact velocity $v_i$ (see inset in Fig. 2(b) and appendix).

### 3.3 Validation of the model

Fig. 3 compares residual projectile kinetic energy from simulations with theoretical predictions, validating our model across varying projectile radii and velocities. The simple model successfully captures the scaling behavior with $R_p$. However, there is a small discrepancy between the simple model proposed here and the simulation outcomes. Fig. 2(a) and 3 shows that for the values investigated in our work, as the impact velocity and the projectile radius increase, the dissipated energy does not approach $\alpha$ but rather a smaller value. Although this slight discrepancy ($\sim$4%) exists—likely due to unmodeled thermal and elastic wave dissipation mechanisms—the agreement remains robust.

Fig. 4(a) confirms strong agreement between the proposed model and simulation results. Minor discrepancies likely result from local thickness variations. Increased kinetic energy absorption reduces agreement, suggesting deviation from the localized fracture assumption. Similarly, longer polymer chains tend to distribute damage more broadly, resulting in slight deviations from the model, as shown in the inset of Fig. 4(a). This deviation would be slightly enhanced if bond scission were included in the polymer model.[30]

Fig. 4(b) shows dissipated energy increases with film thickness for constant projectile mass. Selecting representative upper and lower $\beta$ bounds at the lowest thickness achieves good agreement with simulation data. Agreement declines as maximum dissipation ($v_r = 0$) is approached. The inset supports linear scaling of $E_d$ with film thickness $H$ at nanoscale. At higher velocities we observe a slight increase of $E_d$ with $H$, but this effect remains minor and does not compromise the prediction of eqn (7).

### 3.4 Specific puncture energy

Besides the dissipated (or residual) kinetic energy, another relevant metric in ballistic impact experiments is the specific puncture energy,[31,32] defined as:

$$E_p^* = \frac{1}{2}\frac{m_p}{m_f}v_i^2\left[1-\left(\frac{v_r}{v_i}\right)^2\right] = \frac{1}{2}\alpha v_i^2 + \beta(v_i, N)\frac{2\alpha}{R_p}. \quad (8)$$

Note that, despite its name, $E_p^*$ has the dimensions of velocity squared rather than energy and quantifies the stoppage power of the film per unit of mass. Fig. 5 illustrates that both

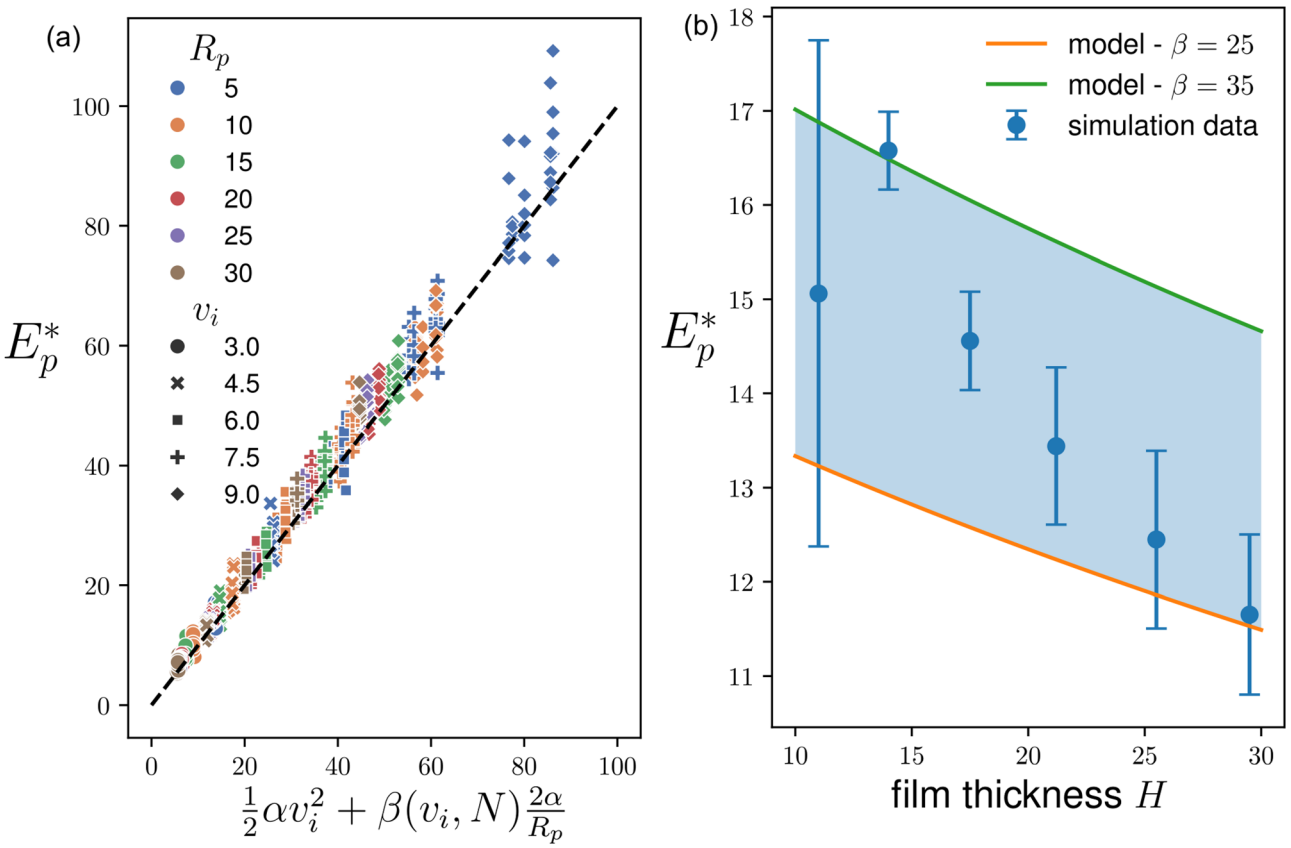


Fig. 5 (a) Specific puncture energy ($E_p^*$) from simulations compared with eqn (8), using velocity and chain-length-dependent $\beta(v_i,N)$. (b) Specific puncture energy as a function of film thickness for projectile mass $m_p$ = 8000.

 

forms of the proposed theoretical expression match well with simulation outcomes, confirming the robustness of our simplified modeling approach. For clarity, Fig. 5 presents the same dataset as Fig. 4 but recast in terms of the specific puncture energy representation.

Recent LIPIT simulations of polymeric thin films by Zhu *et al.*[33] reported a phenomenological scaling $E_p^* \propto H^{-1/2}$. In the present work, we propose a linear scaling with $\alpha$. When the projectile mass is constant, as in Zhu *et al.*'s simulations, both scalings are compatible with our data, however eqn (7) and (8) are more easily interpreted in terms of geometry.

## 4 Discussion and conclusions

As pointed out by Meng and Keten, the energy absorbed through tearing mechanisms is not negligible in ballistic impacts on polymer thin films.[16] Here, the parameter $\beta(v_i,N)$ is introduced to quantify accurately the energy dissipated during this process. This parameter has units of $\sigma^3/\tau^2$, and $\beta(v_i,N)\rho$ can be interpreted as surface energy. It is expected that $\beta(v_i,N)$ correlates with fracture toughness or yield stress, both of which depend similarly on shear rate and molecular weight, represented in this study by the impact velocity $v_i$ and the chain length $N$, respectively. Previous studies have highlighted the relationship between yield stress, toughness, and ballistic energy dissipation in thin films,[11,34] further supporting our interpretation of $\beta(v_i,N)$ as a measure of a film's intrinsic resistance to fracture and plastic yielding under high-rate deformation. Nevertheless, since ballistic tests inherently differ from conventional mechanical tests, direct quantitative comparisons remain challenging.

In summary, we presented a combined computational and theoretical approach to investigate energy dissipation mechanisms in ballistic impacts on polymer thin films at the nanoscale. By explicitly accounting for the energy dissipated through localized tearing around the projectile rim and kinetic energy transfer, we derived, for the first time, an expression capable of accurately describing energy dissipation across a broad range of impact velocities and chain lengths. This work provides insights valuable for the design and optimization of novel polymeric materials intended for ballistic protection applications.

## Author contributions

L. R. G. designed the study. L. R. G. and J.-L. B. supervised the project. N. A. G. produced the samples using the pseudo-continuum model. L. O. and G. C. conducted the impact numerical simulations. L. O. and J.-L. B. create the theoretical model. L. O., J.-L. B. and L. R. G. wrote the manuscript. All authors provided critical feedback and helped shape the research, analysis and manuscript.

## Conflicts of interest

There are no conflicts to declare.

## Data availability

Data for this article, including all simulation results and plots are available at Zenodo **https://doi.org/10.5281/zenodo.15578665**. Additional data related to this paper may be requested from the authors.

## Appendix: behavior of $\beta$

Fig. 6 shows the variation of the impact parameter $\beta$ obtained through the fits in Fig. 2(a) for all $N$. $N$ = 64 and $N$ = 1024

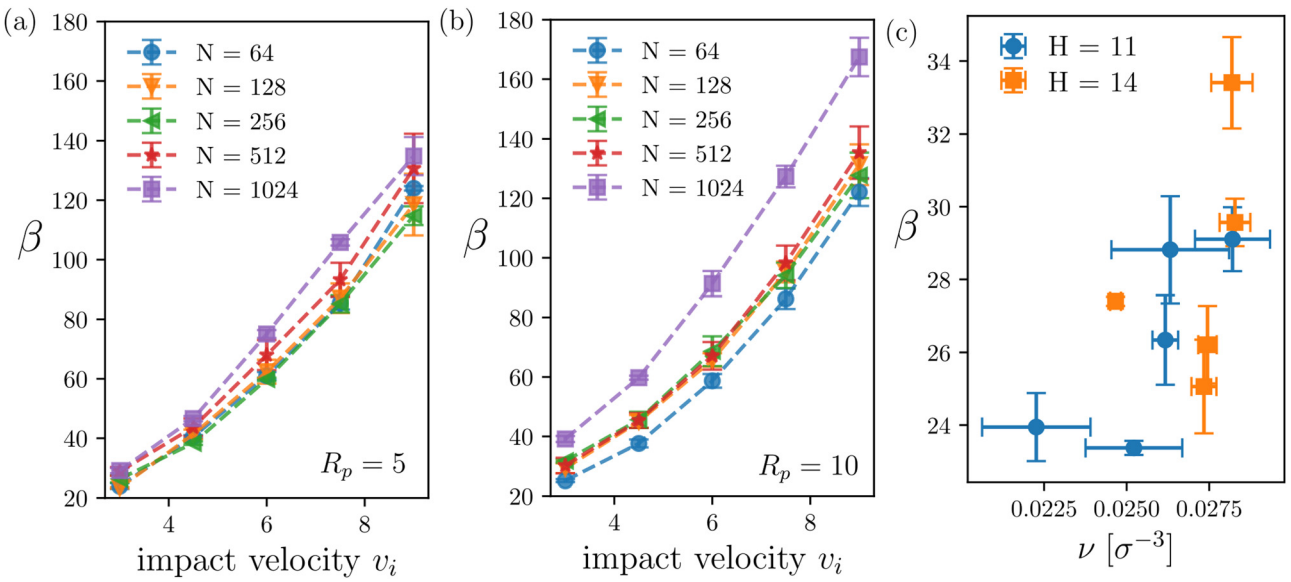


Fig. 6 Panels (a) and (b) show values of $\beta$ over the impacts velocity for different $N$ for $R_p$ = 5 and $R_p$ = 10 respectively ($H$ = 11). Panel (c) shows the values of $\beta$ in terms of the entanglement density $\nu$ for $v_i$ = 3 and $R_p$ = 5.

represent the short-chain length and long-chain limits, respectively, within the range investigated (see inset of Fig. 2). Panel (a) corresponds to the case where the projectile's radius is comparable to the radius of gyration $R_g$ of $N = 64$. Consequently, for all larger values of $N$, $R_g > R_p$. In this regime, the parameter $\beta(v_i, N, R_p = 5)$, and thus the energy absorption, exhibits minimal variation across different chain lengths. Panel (b) presents the values of $\beta(v_i,N,R_p = 10)$ obtained by impacting the same thin films with a projectile of radius 10. In this scenario, $R_p \approx R_g$ for $N = 256$. When $R_g > R_p$, as in the case of $N = 1024$, there is a significant increase in $\beta(v_i,N,R_p = 10)$ due to enhanced polymer tearing. In contrast, for shorter chains where $R_g < R_p$, such as $N = 64$, the value of $\beta$ remains lower.

We also examine the dependence of $\beta$ on the entanglement density, as shown in panel (c). Previous work by Chan *et al.*[9] demonstrated that higher entanglement density enhances energy dissipation. Consistent with their findings, our results reveal a positive correlation between $\beta$ and the entanglement density. The number of entanglements, $Z_{ent}$, was computed using the Z1+ program,[35] and the entanglement density was calculated as $\nu = \frac{Z_{ent}}{L_x L_y H}$. Notably, the values of $\beta = 25$ and $\beta = 35$ provide a suitable fit for the scaling law with $H$ (Fig. 3(b)) where the impacts are at $v = 3$ and the extracted values of $\beta$ for the two thinnest films fall within this range regardless of chain length.

To better understand the physical meaning of the parameter $\beta$, we performed uniaxial tensile deformation simulations of the thin film. The simulations were done in a canonical ensemble at $T = 1$ while keeping the transversal area undeformed. The shear rate was calculated as the $\dot{\varepsilon} = v_i/H$ to emulate the shear rate of the ballistic simulation. After an initial overshoot due to fast deformation, the thin films start to craze and reach a maximum yield stress that is shear rate dependent, as shown in Fig. 7. Beyond the yield point, the true stress decreases monotonically.

The inset of Fig. 7 illustrates that both the toughness, $\Gamma$, and the yield stress, $\sigma_y$, increase with shear rate. Notably, the monotonic increase of these mechanical properties parallels the behavior of $\beta$, suggesting a strong correlation between them. Previous studies have highlighted the relationship between yield stress, toughness, and ballistic energy dissipation in thin films,[11,34] further supporting our interpretation of $\beta$ as a measure of the film's intrinsic resistance to fracture and plastic yielding under high-rate deformation.

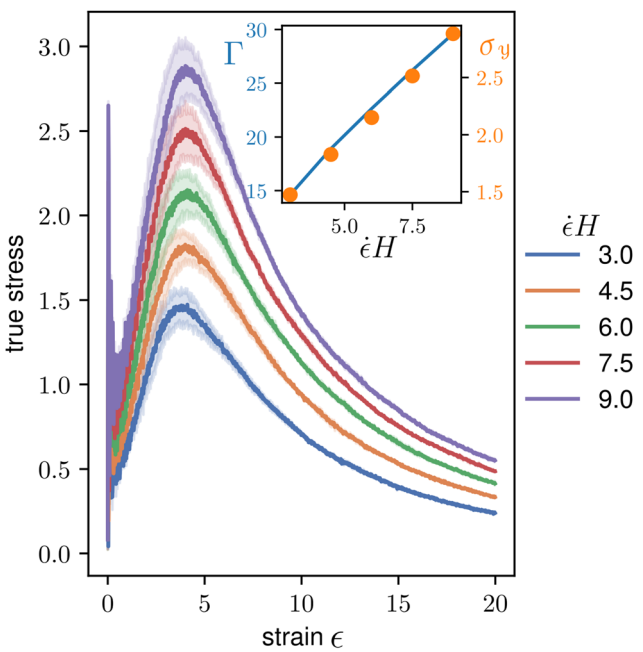


Fig. 7 True stress as a function of strain at various shear rates for nanoscale thin films. The data correspond to three independent samples with $N = 64$ and $H = 11$. The inset (left) shows the toughness $\Gamma$, while the inset (right) presents the yield stress $\sigma_y$ across the range of shear rates studied.

## Acknowledgements

L. O. thanks A. Giuntoli and U. Gürel for their insightful discussions. We acknowledge support from Universidad Nacional del Sur, the National Research Council of Argentina (CONICET), the Fondo para la Investigación Científica y Tecnológica (FONCYT, Grant PICT-2021-1272). L. R. G. acknowledges support from the Alexander von Humboldt Foundation through the George Förster and return fellowships. We acknowledge support from the CNRS international research project "Statistical Physics of Materials". Part of the calculations used the GENCI infrastructure under grant AD010913932R1, and part used the GRICAD infrastructure (**https://gricad.univ-grenoble-alpes.fr**), which is supported by Grenoble research communities. L. O. acknowledges support from the European Union's Horizon Europe research and innovation programme through the Marie Sklodowska-Curie grant agreement No. 101204391.

## Notes and references

1 J.-P. Franc and J.-M. Michel, *Fundamentals of cavitation*, Springer science & Business media, 2006, vol. 76.
2 E. Grossman, I. Gouzman and R. Verker, *MRS Bull.*, 2010, **35**, 41–47.
3 M. Stack, F. Stott and G. Wood, *Wear*, 1993, **162**, 706–712.
4 T. J. Carter, *Eng. Failure Anal.*, 2005, **12**, 237–247.
5 J.-H. Lee, D. Veysset, J. P. Singer, M. Retsch, G. Saini, T. Pezeril, K. A. Nelson and E. L. Thomas, *Nat. Commun.*, 2012, **3**, 1164.
6 R. R. Søndergaard, M. Hösel and F. C. Krebs, *J. Polym. Sci., Part B: Polym. Phys.*, 2013, **51**, 16–34.
7 J. Hyon, O. Lawal, O. Fried, R. Thevamaran, S. Yazdi, M. Zhou, D. Veysset, S. E. Kooi, Y. Jiao and M.-S. Hsiao, *et al.*, *Mater. Today*, 2018, **21**, 817–824.
8 W. Xie and J.-H. Lee, *Macromolecules*, 2020, **53**, 1701–1705.
9 E. P. Chan, W. Xie, S. V. Orski, J.-H. Lee and C. L. Soles, *ACS Macro Lett.*, 2019, **8**, 806–811.
10 J. Cai and R. Thevamaran, *Nano Lett.*, 2020, **20**, 5632–5638.

11 U. Gurel, S. Keten and A. Giuntoli, *ACS Macro Lett.*, 2024, **13**, 302–307.
12 R. F. Recht and T. W. Ipson, *J. Appl. Mech.*, 1963, **30**, 384–390.
13 S. H. Chen, A. J. Souna, C. L. Soles, S. J. Stranick and E. P. Chan, *Soft Matter*, 2020, **16**, 3886–3890.
14 R. Vermorel, N. Vandenberghe and E. Villermaux, *Proc. R. Soc. A*, 2009, **465**, 823–842.
15 N. Vandenberghe and L. Duchemin, *Phys. Rev. E*, 2016, **93**, 052801.
16 Z. Meng and S. Keten, *J. Appl. Mech.*, 2018, **85**, 121004.
17 A. Korolkovas, P. Gutfreund and J.-L. Barrat, *J. Chem. Phys.*, 2016, **145**, 124113.
18 A. Korolkovas, C. Rodriguez-Emmenegger, A. de los Santos Pereira, A. Chenneviere, F. Restagno, M. Wolff, F. A. Adlmann, A. J. Dennison and P. Gutfreund, *Macromolecules*, 2017, **50**, 1215–1224.
19 A. Korolkovas, *Adv. Theory Simul.*, 2018, **1**, 1800078.
20 N. A. Garca and J.-L. Barrat, *Macromolecules*, 2018, **51**, 9850–9860.
21 B. Arman, A. S. Reddy and G. Arya, *Macromolecules*, 2012, **45**, 3247–3255.
22 D. A. Vega, P. Lance, E. Zorzi, R. A. Register and L. R. Gómez, *Soft Matter*, 2023, **19**, 6131–6139.
23 L. Ortellado, D. A. Vega and L. R. Gómez, *Phys. Rev. E*, 2022, **106**, 044502.
24 J. A. Anderson, J. Glaser and S. C. Glotzer, *Comput. Mater. Sci.*, 2020, **173**, 109363.
25 G. S. Grest, M. D. Lacasse, K. Kremer and A. M. Gupta, *J. Chem. Phys.*, 1996, **105**, 10583–10594.
26 M. Murat, G. S. Grest and K. Kremer, *Macromolecules*, 1999, **32**, 595–609.
27 K. Kremer and G. S. Grest, *J. Chem. Phys.*, 1990, **92**, 5057–5086.
28 Including an attractive interaction (by extending the cutoff radius of the Lennard-Jones potential to 2.5 $\sigma$) produces, at most, a $\sim$10% decrease in the residual velocity within the parameter range investigated.
29 A. L. Bowman, E. P. Chan, W. B. Lawrimore and J. K. Newman, *Nano Lett.*, 2021, **21**, 5991–5997.
30 Assuming bond scission occurs only when bond extension exceeds 1.3 simulation units, we have numerically estimated that in the most extreme case ($N$ = 1024, $v_i$ = 9 and $H$ = 11) no more than 2% of bonds (those within the strike area plus one radius of gyration) would reach this threshold. This would alter the projectile's residual velocity by $v_r/v_i \sim 0.02$.
31 J.-H. Lee, P. E. Loya, J. Lou and E. L. Thomas, *Science*, 2014, **346**, 1092–1096.
32 B. Schrauwen, P. Bertens and T. Peijs, *Polym. Polym. Compos.*, 2002, **10**, 259–272.
33 Y. Zhu, A. Giuntoli, N. Hansoge, Z. Lin and S. Keten, *J. Mech. Phys. Solids*, 2022, **161**, 104808.
34 A. Giuntoli and S. Keten, *Cell Rep. Phys. Sci.*, 2021, **2**, 100596.
35 M. Kröger, J. D. Dietz, R. S. Hoy and C. Luap, *Comput. Phys. Commun.*, 2023, **283**, 108567.